Cascaded ring resonator and Mach-Zehnder interferometer with a Sagnac loop for Vernier-effect refractive index sensing

Original Citation:
Cascaded ring resonator and Mach-Zehnder interferometer with a Sagnac loop for Vernier-effect refractive index sensing / Troia, B.; De Leonardis, F.; Passaro, V. M. N.. - In: SENSORS AND ACTUATORS. B, CHEMICAL. - ISSN 0925-4005. - STAMPA. - 240:(2017), pp. 76-89. [10.1016/j.snb.2016.08.095]

Published version
DOI:10.1016/j.snb.2016.08.095

Publisher:

Cascaded ring resonator and Mach-Zehnder interferometer with a Sagnac loop for Vernier-effect refractive index sensing

Benedetto Troia, Francesco De Leonardis, and Vittorio M. N. Passaro*

Department of Electrical and Information Engineering, Politecnico di Bari, Via E. Orabona n° 4, 70125 Bari, Italy

*Corresponding author: vittorio.passaro@poliba.it

Abstract

In this paper, we propose a novel photonic integrated sensor characterized by the cascade of a ring resonator (RR) and an interferometer architecture consisting of a Mach-Zenhder interferometer (MZI) and a Sagnac loop (RR-MZI-Sagnac). We present the modelling and detailed guidelines for the design of such devices that are assumed to be fabricated on CMOS-compatible silicon-on-insulator (SOI) platforms. Ultra-high refractive index (RI) sensing performance such as wavelength sensitivities greater than 2.5×10^3 μm/RIU and limits of detection (LOD) down to 1×10^{-8} RIU can be achieved by employing the Vernier effect in the near-infrared (NIR), around the wavelength of 1.55 μm. Furthermore, we demonstrate, theoretically, that the novel RR-MZI-Sagnac Vernier devices can operate better than the most performing state-of-the-art Vernier sensors characterized by cascaded RR and MZI (RR-MZI). In fact, an operating bandwidth that is half that requested by the RR-MZI devices is exhibited when balanced MZIs are designed in both configurations, still preserving similar RI sensing performance. Alternatively, double RI sensing performance can be achieved by RR-MZI-Sagnac Vernier sensors with respect to RR-MZI devices when unbalanced MZIs are considered in both the Vernier configurations, exhibiting the same operating bandwidths. Finally, simulations reveal that ammonia (NH_3) concentrations in the 0-30,000 ppm range and carbon dioxide (CO_2) traces lower than 5,000 ppm can be detected in DI water and air, respectively.

1. Introduction

Photonic integrated sensors has attracted a great interest in the last decade due to the very high sensitivity and selectivity achievable in chemical and biochemical sensing, and other unique features such as, immunity to electromagnetic interferences, compatibility with microelectronic fabrication facilities, low-cost and large scale production, small footprints, integration with microfluidics systems, real-time spectroscopy in the MIR, label-free and lab-on-a-chip sensing functionalities [1, 2]. Nowadays, pioneering research efforts are carried out in order to further improve sensor selectivity and accessibility to multiple analytes in complex mixtures. In this context, the Vernier effect has been demonstrated as a very useful technique to enhance RI sensing performance of chemical and biochemical integrated photonic sensors [3, 4].

The Vernier principle consists in using two measurement scales with slightly different periods, where one scale is fixed and the other can slide over the former. By properly setting the ratio between the scale periods, the overall resolution of the system can be enhanced G_v times, with G_v the Vernier gain, compared to the measurement resolutions achievable by each of the measurement scales considered alone. Actually, this principle has been experimentally demonstrated in integrated photonic sensors by cascading two RRs [5-10], two MZIs [11], or combinations of both [12]. Practically, one of the cascaded devices should be covered by an insulating layer and acting as a filter, thus exhibiting a fixed wavelength-dependent transmittance. Conversely, the other device should be exposed to the sensitive area and acting as a sensor, whose transmittance can slide as a function of the sensing activities.

When working with Vernier sensors, the cascaded devices should be properly designed in order that their FSRs (i.e. the periods of the two scales said above) satisfy the condition for operating in the second regime of the Vernier effect, i.e., $\Delta FSR = |FSR_1 - FSR_2| < \Delta\lambda_{FWHM(1,2)}$ [8]. In particular, FSR_1 is the FSR of the filter, while FSR_2 is the FSR of the sensor, thus the device directly exposed to the sensitive area, where the analyte to be detected is located and sensing functionalities can occur. Then, $\Delta\lambda_{FWHM(1,2)}$ is the minimum linewidth at the full-width-at-half-maximum (FWHM) among resonant peaks of both cascaded devices. Finally, the Vernier gain, G_v, is equal to the ratio $FSR_1/\Delta FSR$, the Vernier sensitivity, $S_{\lambda,v}$, is directly proportional to G_v, while the lower ΔFSR the lower the Vernier LOD, LOD_v.

Useful plots that show how the mentioned Vernier figures of merit vary as a function of ΔFSR can be analysed in [13]. In particular, a number of FSR_1 and FSR_2 combinations can be selected to achieve different values of ΔFSR, and, even though the gain G_v tends to infinity when $\Delta FSR \rightarrow 0$ (excluding the degenerate condition $\Delta FSR = 0$, when $FSR_1 = FSR_2$), the smaller ΔFSR the larger the overall Vernier FSR, FSR_v, that characterizes the Vernier transmittance envelope, with $FSR_v = (FSR_1 \times FSR_2)/\Delta FSR$. In other words, the higher the RI sensing performance, particularly, the Vernier wavelength sensitivity, the larger FSR_v.

We propose in Table 1 a useful comparison among some photonic integrated Vernier sensors operating in the NIR, listing their sensing performance, thus G_v, $S_{\lambda,v}$, and LOD_v, and the optical parameters, FSR_1, FSR_2, ΔFSR, and FSR_v.

Table I
RI sensing performance and optical parameters of some silicon Vernier photonic sensors demonstrated experimentally in the NIR.

Ref.	FSR_1 (nm)	FSR_2 (nm)	ΔFSR (pm)	G_v	FSR_v (nm)	$S_{\lambda,v}$ (µm/RIU)	LOD_v (RIU)
[5]	0.6560	0.6290	0.0270	24.3	15.28	1.30	5.0×10^{-4}
[6]	2.1800	2.1000	0.0800	27.2	57.22	460.00	4.8×10^{-6}
[7]	0.7035	0.7082	0.0047	149.7	106.00	24.30	$< 7.0\times10^{-4}$
[8]	0.2196	0.2114	0.0082	26.8	5.66	2.17	8.3×10^{-6}
[12]	1.0400	0.9910	0.0490	21.2	21.03	21.50	$< 10^{-4}$

With reference to Table I, a Vernier wavelength sensitivity of 24.3 µm/RIU has been achieved with a Vernier gain as high as 149.7 and a FSR_v as large as 106 nm [7], while a higher sensitivity $S_{\lambda,v}$ = 460 µm/RIU has been achieved with shorter Vernier FSR, FSR_v = 57.22 nm, and a lower gain, G_v = 27.2 [6]. This confirms that the trends previously figured out are valid only for a specific Vernier device, where FSR_1 and FSR_2 can be varied to achieve the required performance, and not when comparing different Vernier sensors, based, for example, on different waveguides, material platforms or filter and sensor devices. In this context, it is worth specifying that among Vernier sensor architectures based on cascaded RRs, MZIs, and combinations of both (RR-MZI), the latter allow similar performance of the former configurations to be achieved with lower gains G_v and, thus, lower Vernier FSR_v, as demonstrated theoretically in [14], and by comparing [12] and [7] in Table I.

In summary, the inverse nonlinear relationship between FSR_v and ΔFSR can represent a strong limitation when Vernier sensors are requested to exhibit ultra-high RI sensing performance for detecting, for example, part-per-billion (ppb) or part-per-trillion (ppt) gas traces or concentrations of biochemical species of the order or femtomoles (fM). Practically, ultra-high performance Vernier sensors with very large FSR_v (e.g., larger than 100 nm) require i) the use of ultra-broadband photodetectors, ii) grating couplers characterized by ultra-broad bandwidths and high coupling efficiency that are challenging to be achieved, iii) ultra-broadband, low-dispersion, and low-attenuation fibre optics, as well as iv) ultra-broadband tunable lasers that can make the experimental setup costly and bulky. Finally, when Vernier transmittance are characterized by FSR_v of hundreds of nm chromatic dispersion phenomena can affect dramatically sensing functionalities, resulting in very complex wavelength readout schemes.

In this paper, we report on the investigation of a new Vernier-effect based sensor characterized by the cascade of a RR and an interferometer architecture based on a MZI and a Sagnac loop, named as RR-MZI-Sagnac, and sketched in Fig. 1.

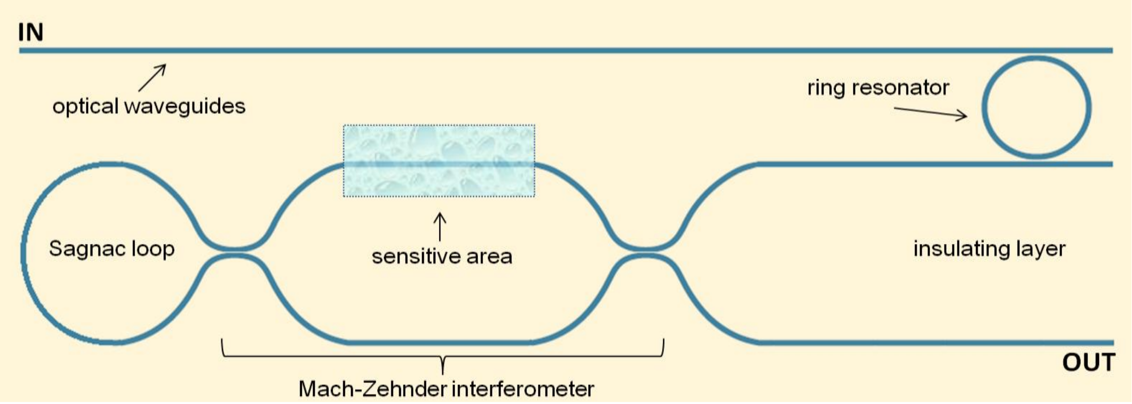

Fig. 1. Schematic of the RR-MZI-Sagnac Vernier sensor.

In particular, we demonstrate, theoretically, that by implementing two different design approaches consisting in the use of balanced or unbalanced MZI-Sagnac configurations, state-of-the-art RI sensing performance demonstrated in RR-MZI Vernier sensors proposed in [14] can be achieved in half their bandwidths or, alternatively, double Vernier wavelength sensitivities, $S_{\lambda,v}$, and Vernier LODs, LOD_v, can be exhibited by RR-MZI-Sagnac within the same bandwidths of RR-MZI Vernier architectures.

The paper is organized as follows. In Section 2, we present the modelling of the proposed device, reporting the fundamental design equations. In Section 3, we demonstrate the advantages of the RR-MZI-Sagnac Vernier sensors with respect to state-of-the-art RR-MZI Vernier sensors assumed to be fabricated on SOI technology platform and operating in the NIR. Finally, Section 4 summarizes the conclusions.

2. Modelling

In this Section we present the modelling of the novel RR-MZI-Sagnac Vernier photonic sensor. To this purpose, an important contribution has been reported by C. Han *et al.* in the literature [15]. Authors propose a transfer matrix method to model the MZI-Sagnac interferometric architecture assumed to be based on optical fibres. In this work, we propose an extended version of the model, introducing a RR to generate the Vernier effect, taking into account waveguide propagation losses, the attenuation of DCs, and reporting fundamental equations to estimate enhanced RI sensing performance, accurately. Finally, we investigate the influence of the counter-propagating signals generated in the Sagnac loop on the overall device operation.

The schematic of the RR-MZI-Sagnac Vernier device shown in Fig. 2 can be considered to investigate the mathematics developed in the following.

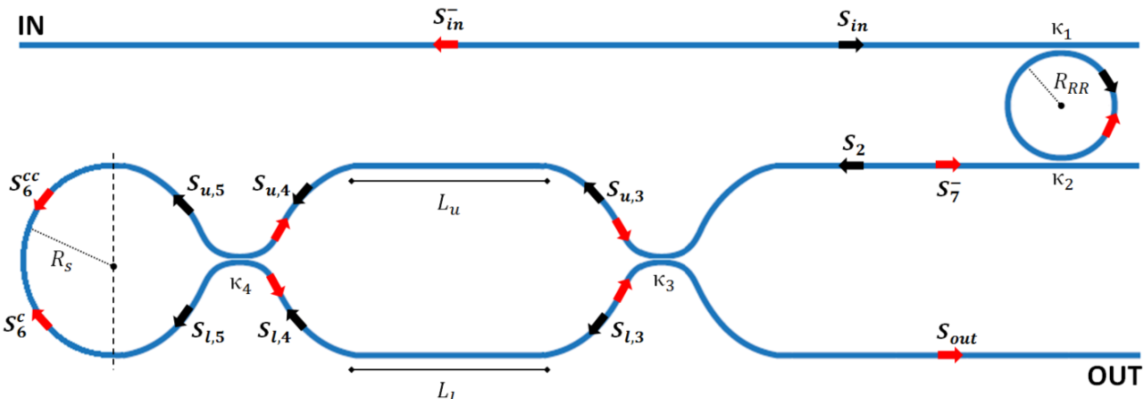

Fig. 2. Schematic of the RR-MZI-Sagnac Vernier sensor with input and output ports labelled in, optical signal propagation paths indicated by the red and black arrows, DC power coupling coefficients, κ_1, κ_2, κ_3, and κ_4, and fundamental geometrical parameters, R_s, L_u, L_l, R_{RR}.

With reference to Fig. 2, S_{in} is the input signal at the input port of the device that is coupled to the RR by means of the first DC characterized by a power coupling coefficient κ_1. Then, by following the signal propagation indicated by the black arrows in Fig. 2, it is possible to calculate the signal S_2 at the drop port of the add-drop RR by using Eq. (1):

$$S_2 = S_{in}\frac{-\alpha_{loss,RR}r_1r_2e^{j\frac{\phi_{RR}}{2}}}{1-\alpha_{loss,RR}t_1t_2e^{j\phi_{RR}}} \tag{1}$$

In Eq. (1), $\phi_{RR} = \beta_{RR}L_{RR}$ is the phase shift that the signal undergoes propagating into the RR characterized by the roundtrip length L_{RR}, with $\beta_{RR} = (2\pi/\lambda)n_{g,RR}$ the propagation constant, $n_{g,RR}$ the group index of the optical waveguide mode at the operating wavelength λ. Furthermore, the parameter $\alpha_{loss,RR}$ can be calculated as $\alpha_{loss,RR}^2 = e^{-\alpha L_{RR}}$ with α the RR waveguide power attenuation coefficient measured in cm^{-1}. Finally, $t_i = \sqrt{1-\kappa_i}$ and $r_i = \sqrt{\kappa_i}$ are the transmission and coupling coefficients of the i-th DC ($i = 1, 2$), respectively [16].

The signal S_2 is the input at the lower arm port of the MZI-Sagnac architecture. In particular, the presence of the third DC indicated in Fig. 2 with its power coupling coefficient, κ_3, determines a part of the signal S_2, i.e., $S_{u,3}$, to be coupled to the upper arm of the MZI, while a part of the same signal, i.e., $S_{l,3}$, is transmitted and propagates in the lower arm. In this context, it is worth specifying that these two signals undergo a different phase shifts when the lengths of the upper and lower arms, let us indicate them as L_u and L_l, respectively, are different, but also when the condition $L_u = L_l$ is satisfied. Indeed, the group indices of the signals propagating into the upper and lower arms, $n_{g,u}$ and $n_{g,l}$, respectively, are different, being the upper waveguide exposed to the sensitive area (e.g., covered by deionized water (DI) or air), and the lower waveguide isolated by a cladding material (e.g., Teflon, SU8, SiO_2). In summary, the balanced and unbalanced MZI configurations can be distinguished when $L_u = L_l$ and $L_u \neq L_l$, respectively, and the condition $n_{g,u} \neq n_{g,l}$ is always satisfied for the motivations said above. Consequently, we name $\phi_u = \beta_u L_u$ and $\phi_l = \beta_l L_l$ the phase shifts that the signals $S_{u,4}$ and $S_{l,4}$ undergo propagating in the upper and lower arms of the interferometric architecture, respectively.

At this stage of the analysis, it is worth noting that the signal $S_{u,4}$ takes into account the relevant information of the sensing functionalities occurring into the sensitive area as it is assumed on the upper arm of the MZI. Actually, by considering both RI homogeneous and surface sensing principles, a localized RI perturbation of the waveguide cladding material (i.e., Δn_c) or, similarly, a variation of the functionalized biochemical layer thickness (t_{ad}) due to the selectively adsorption of specific analytes on the waveguide surface in the sensitive area, can be transduced into a variation of the effective index of the optical mode that propagates in the upper waveguide arm, i.e., $n_{eff,u}$, as indicated by the homogeneous and surface waveguide sensitivities defined as $S_h = \partial n_{eff,u}/\partial n_c$ and $S_s = \partial n_{eff,u}/\partial t_{ad}$, respectively [17].

The fourth DC characterized by the power coupling coefficient, κ_4, allows the signals $S_{u,4}$ and $S_{l,4}$ to be coupled to the Sagnac loop. Consequently, the new signals $S_{u,5}$ and $S_{l,5}$ undergo the same phase shift equal to ϕ_s and dependent on the Sagnac loop radius, let us name it R_s. The Sagnac loop radius does not influence the overall device operation, thus it can be set at a specific value that allows low bend losses to be achieved, depending on the specific technology platform employed. Moreover, the counter-propagating optical signals, i.e., the clockwise, S_6^c, and the counter-clockwise, S_6^{cc}, travel back from the Sagnac loop to the fourth DC and then to the third DC through the upper and lower arms, undergoing additional phase shifts similarly as explained previously. In particular, it is worth noting that light-analyte interactions are also enhanced due to the multiple forward and backward signal propagation paths into the sensitive area.

In the following, we present the fundamental equations for calculating the forward and backward signals at a desired section of the RR-MZI architecture. In particular, the transfer matrix method inherent to the forward propagating signals is described in Eqs. (2)-(5):

$$\begin{bmatrix} S_{u,3} \\ S_{l,3} \end{bmatrix} = q_3 \begin{bmatrix} t_3 & -jr_3 \\ -jr_3 & t_3 \end{bmatrix} \begin{bmatrix} S_2 \\ 0 \end{bmatrix} = q_3 T_{DC_3} \begin{bmatrix} S_2 \\ 0 \end{bmatrix} \tag{2}$$

$$\begin{bmatrix} S_{u,4} \\ S_{l,4} \end{bmatrix} = \begin{bmatrix} \alpha_{loss,u} e^{j\phi_u} & 0 \\ 0 & \alpha_{loss,l} e^{j\phi_l} \end{bmatrix} \begin{bmatrix} S_{u,3} \\ S_{l,3} \end{bmatrix} = T_{MZI} \begin{bmatrix} S_{u,3} \\ S_{l,3} \end{bmatrix} \tag{3}$$

$$\begin{bmatrix} S_{u,5} \\ S_{l,5} \end{bmatrix} = q_4 \begin{bmatrix} t_4 & -jr_4 \\ -jr_4 & t_4 \end{bmatrix} \begin{bmatrix} S_{u,4} \\ S_{l,4} \end{bmatrix} = q_4 T_{DC_4} \begin{bmatrix} S_{u,4} \\ S_{l,4} \end{bmatrix} \tag{4}$$

$$\begin{bmatrix} S_6^c \\ S_6^{cc} \end{bmatrix} = \begin{bmatrix} 0 & \alpha_{loss,s} e^{j\phi_s} \\ \alpha_{loss,s} e^{j\phi_s} & 0 \end{bmatrix} \begin{bmatrix} S_{u,5} \\ S_{l,5} \end{bmatrix} = T_{Sagnac} \begin{bmatrix} S_{u,5} \\ S_{l,5} \end{bmatrix} \tag{5}$$

In Eqs. (6) and (8), coefficients q_i $(i = 3, 4)$ are the coupling loss factors for the third and fourth DCs, ranging between 0 (infinite coupling loss) and 1 (null coupling loss). In particular, similar coefficients have been taken into account also for the first and second RR DCs (see Eq. 5), but lossless DCs have been assumed in simulations, thus $q_i = 1$ $(i = 1, 2, 3, 4)$. Furthermore, the propagation loss coefficients $\alpha_{loss,u}$, $\alpha_{loss,l}$, and $\alpha_{loss,s}$ in Eqs. (7) and (9) are defined similarly as $\alpha_{loss,RR}$ and allow propagation losses occurring in the upper and lower MZI arms as well as in the Sagnac loop, respectively, to be included in simulations.

The transfer matrix method can be applied similarly to calculate the counter-propagating signals as shown in Eq. (6). In particular, the relevant contributions worth being analysed are the signal at the output port of the RR-MZI-Sagnac architecture, which is also useful to determine the overall sensor transmittance, and the signal that goes back to the input port through the cascaded RR, namely S_{in}^-.

$$\begin{bmatrix} S_7^- \\ S_{out} \end{bmatrix} = q_3 DC_3 T_{MZI} q_4 DC_4 \begin{bmatrix} S_6^c \\ S_6^{cc} \end{bmatrix} \tag{6}$$

In Eq. (6), S_{out} is the optical signal at the sensor output port and allows the overall sensor transmittance S_{out}/S_{in} to be calculated as a function of all the geometrical and physical parameters. Furthermore, S_7^- is the backward signal that counter-propagates back to the interferometer architecture input port on the upper arm. Finally, the overall backward contribution at the sensor input port, S_{in}^-, can be estimated by using Eq. (1) and considering S_7^- instead of S_{in} in it.

2.1 Refractive index sensing performance of MZI-Sagnac and Vernier RR-MZI-Sagnac sensors

In this subsection, we report the fundamental equations that allow accurate estimations of RI sensing performance to be calculated. In particular, it is worth focusing our analysis on the sensing device, i.e., the interferometric architecture based on a MZI and a Sagnac loop, i.e., MZI-Sagnac. The choice of selecting the device said above as the sensing element instead of the RRs has been well demonstrated by M. La Notte *et al.* [14], evidencing how the wavelength sensitivity, S_λ, of a typical MZI can be G_s times higher than that of an add-drop RR. In particular, G_s can be calculated by Eq. (7):

$$G_s = \frac{n_{g,RR}}{n_{g,u} - \eta n_{g,l}} \tag{7}$$

In Eq. 7, η is the ratio of the reference and sensing arm lengths defined as L_l/L_u. The assumption that should be done in order to quantify the gain G_s correctly is that the RR and the sensing arm of the MZI are characterized by the same waveguides (i.e., identical waveguide sensitivities, S_w either an homogeneous sensitivity, S_h, or a surface sensitivity, S_s) and are exposed to the same RI cladding (i.e., $n_{g,RR} = n_{g,u}$). Then, the expression of G_s becomes $1/(1 - \eta\,(n_{g,l}\,/n_{g,u}\,))$.

Actually, the MZI wavelength sensitivity, S_λ, that is still the same if a Sagnac loop characterizes the MZI, can be calculated as in Eq. (8), where all the parameters have already been defined with the exception of λ_{peak} that is the central wavelength of a peak of the sinusoidal wavelength-dependent MZI transmittance.

$$S_\lambda = \frac{\Delta\lambda}{\Delta n_c} = \frac{S_w L_l \lambda_{peak}}{n_{g,u} L_u - n_{g,l} L_l} \tag{8}$$

In this context, it is worth reporting a useful expression for the LOD that is valid when working with resonant peaks (e.g., add-drop RR or MZI transmittance resonant peaks), if the thermal noise is not a limiting factor and the resonant linewidth at the FWHM, $\Delta\lambda_{FWHM}$, is much greater than the resolution of the optical spectrum analyser (OSA) used in the experiments (note that typical OSA resolutions can be lower than 50 pm) [18, 19]:

$$LOD \approx \frac{1}{S_\lambda} \frac{\Delta\lambda_{FWHM}}{1.5(SNR)^{0.25}} \tag{9}$$

In Eq. (9), SNR is the signal-to-noise-ratio of the measurements valuated at the minimum of the wavelength-dependent transmittance and expressed in linear units. Furthermore, the expression of the LOD indicates that the higher S_λ the lower the minimum cover RI variation, Δn_c, or, similarly, the minimum biochemical layer thickness variation, Δt_{ad}, that can be detected. Although this analysis is in perfect agreement with the motivation of selecting the MZI over the add-drop RR, it is worth specifying that $\Delta\lambda_{FWHM}$ of a MZI peak is always wider than that of a RR peak, thus resulting in an decrease of the LOD especially when the quality factor, Q, of the resonant cavity is in the range of $10^4 \div 10^8$. Indeed, high Q-factors are particularly suitable for sensing applications as the effective interaction length that a resonant mode undergoes into the cavity is proportionally to Q as $L_{eff} = (Q\lambda_{res})/(2\pi n_{g,RR})$ [20], with λ_{res} a cavity resonant wavelength. Overall, a compromise between S_λ and $\Delta\lambda_{FWHM}$ should be made as a function of the specific sensing application and required performance, especially in the case of Vernier-effect-based photonic sensors, where wavelength sensitivities of the order of hundreds of μm/RIU and $\Delta\lambda_{FWHM}$ as large as hundreds of nm can occur [3, 14].

We report the fundamental equations, i.e., Eqs. (10)-(11), that allow the Vernier LOD, LOD_v, and the Vernier wavelength sensitivity, $S_{\lambda,v}$, of RR-MZI-Sagnac and RR-MZI Vernier sensors to be calculated:

$$LOD_v = \frac{\Delta FSR(n_{g,u} - \eta n_{g,l})}{\lambda_{peak} S_w} \tag{10}$$

$$S_{\lambda,v} = S_\lambda G_v \tag{11}$$

In conclusion, it is worth noting that specific RI sensing performance can be achieved as a function of the sensing applications to be performed, by properly designing the overall photonic device in order to exhibit a desired Vernier gain, G_v, as also demonstrated in the case of SOI cascaded RRs Vernier sensors designed for methane (CH_4) and ethane (C_2H_6) sensing at the mid-infrared (MIR) wavelength of 3.39 μm [13].

3. Numerical results and discussions

In this Section, we demonstrate the advantages of using the RR-MZI-Sagnac Vernier configuration with respect to state-of-the-art RR-MZI Vernier sensors, which are the most performing Vernier configurations demonstrated by now in the literature [14].

Hereafter, we consider a SOI wire waveguide characterized by a width, W = 320 nm, a height H = 220 nm, and a buried oxide (BOX) thickness layer of 2 μm, as also considered in [14]. The assumed SOI waveguide can be fabricated by means of CMOS-compatible e-beam lithography and ICP etching tools. Furthermore, both the cascaded RR and the MZI-Sagnac interferometric architecture are assumed to be based on the SOI wire waveguide covered by a 1-μm-thick SiO_2 cladding layer with the only exception of the sensitive area, where DI water is considered as the cover medium (see Fig. (1)). Moreover, it is worth specifying that simulations have been performed by using a mode solver based on a finite element method (FEM) [21], where an overall computational domain area of 8 μm^2 and more than 90,000 mesh elements have been set. In particular, custom-made codes have also been developed in the FEMLAB platform to perform geometrical and optical multi-parametric simulations, where Sellemeir's equations for silicon [22] and its oxide [23] have also been implemented to take into account the material chromatic dispersion in the NIR wavelength range of 1250-1850 nm. Furthermore, waveguide single-mode operation and transverse-electric (TE) polarization of the optical mode have been considered as optimal conditions for sensing purposes. Finally, we report in Table II the fundamental optical parameters calculated, i.e., the waveguide group and effective indices with DI water (H_2O) [24] and SiO_2 claddings, n_{eff,H_2O}, n_{eff,SiO_2}, and n_{g,H_2O}, n_{g,SiO_2}, respectively, the homogeneous sensitivity of the waveguide covered by DI water, S_{h,H_2O}, and the optical field confinement in the sensitive area, Γ_{c,H_2O} [17].

Table II

Optical parameters of the optimized SOI wire waveguides simulated at the wavelength of 1.55 μm.

Parameters	Simulated values
n_{eff,H_2O}	1.8589
n_{eff,SiO_2}	1.9227
n_{g,H_2O}	4.4521
n_{g,SiO_2}	4.3060
S_{h,H_2O}	0.5551
Γ_{c,H_2O}	49.86%

With reference to Table II, it is worth noting that the optimized SOI wire waveguide allows almost 50% of the overall optical E-field intensity to be confined into the sensitive area, where the analyte to be detected is concentrated. Also, an homogeneous sensitivity of 0.5551 allows more than half of the localized cover RI perturbation, Δn_c, to be transduced into an effective RI variation, Δn_{eff}, thus providing an efficient sensing functionality. Actually, although more sensitive waveguides (i.e., $S_h \approx 1$) such as slot waveguides [17], membrane or suspended wave-guiding structures [25] can be used to further enhance overall sensing performance, the optimized SOI wire waveguide proposed in [14] has been selected in order to better compare our device performance with the state-of-the-art RR-MZI sensors. Finally, a cross-sectional view of the SOI wire waveguide covered by DI water is shown in Fig. 3, where the countour map of the spatial distribution of the E_x-field component of the quasi-TE polarized optical mode is simulated at λ = 1.55 μm.

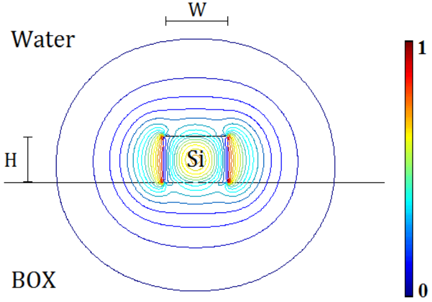

Fig. 3. Countour map of the fundamental quasi-TE polarized optical mode spatial distribution into the optimized SOI wire waveguide (W= 320 nm, H = 220 nm) at the operating wavelength, λ = 1.55μm.

The analysis of the RR-MZI-Sagnac Vernier sensor can start by investigating the operation of the MZI-Sagnac interferometric architecture as a stand-alone device, i.e., without the cascaded RR. Furthermore, we report a useful comparison between the MZI-Sagnac architecture considered here and a typical MZI sensor characterized by the same DCs as sketched in Fig. 4.

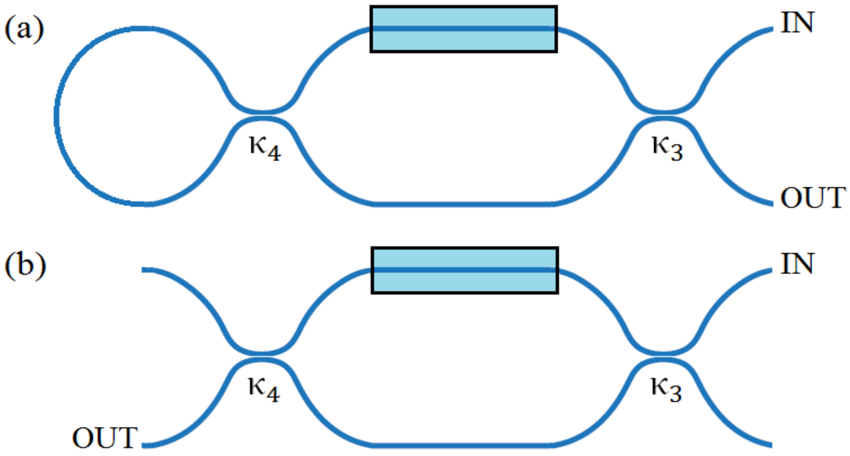

Fig. 4. (a) Schematic of the MZI-Sagnac interferometric architecture with DC power coupling coefficients κ_3 and κ_4. (b) A typical MZI sensor configuration characterized by the same DCs as in (a).

In Figs. 4(a) and 4(b), both the devices are assumed to be based on the optimized SOI waveguide shown in Fig. 3. In particular, the overall devices are covered by a 1-μm-thick SiO_2 cladding layer with the only exception of the sensitive areas located at the upper arms of each configuration. As an example, we have assumed that L_u = L_l = 500 μm in both the devices (a) and (b), thus resulting in balanced MZIs with input and output ports as labelled in the same Figure. Finally, the transmittances of the devices have been calculated as a function of different sets of DC power coupling coefficients, κ_3 and κ_4, i.e., (κ_3 = 0.067, κ_4 = 0.25), (κ_3 = 0.5, κ_4 = 0.1464) and (κ_3 = 0.25, κ_4 = 0.25). The results for the MZI-Sagnac and MZI devices are plotted in Figs. 5(a) and 5(b), respectively.

In Figs. 5(a) and 5(b), it is possible to see that, as also demonstrated in [15], the MZI-Sagnac wavelength-dependent transmittance depends dramatically on specific values of the DC coupling coefficients κ_3 and κ_4. Also, when the power coupling coefficient pairs (κ_3 = 0.067, κ_4 = 0.25), and (κ_3 = 0.25, κ_4 = 0.25) are taken into account, then FSR of the transmittances, namely FSR_1, is the same and equal to 32.89 nm around the wavelength of 1.55 μm. In particular, it is worth specifying that Eq. (12) can be used for estimating accurately the FSRs of both the devices, where $n_{g,u}$ = n_{g,H_2O}, $n_{g,l}$ = n_{g,SiO_2}, and λ_{peak} is the operating wavelength at which a peak of the periodic wavelength-dependent transmittance is centred.

$$FSR = \frac{\lambda_{peak}^2}{(L_u n_{g,u} - L_l n_{g,l})} \tag{12}$$

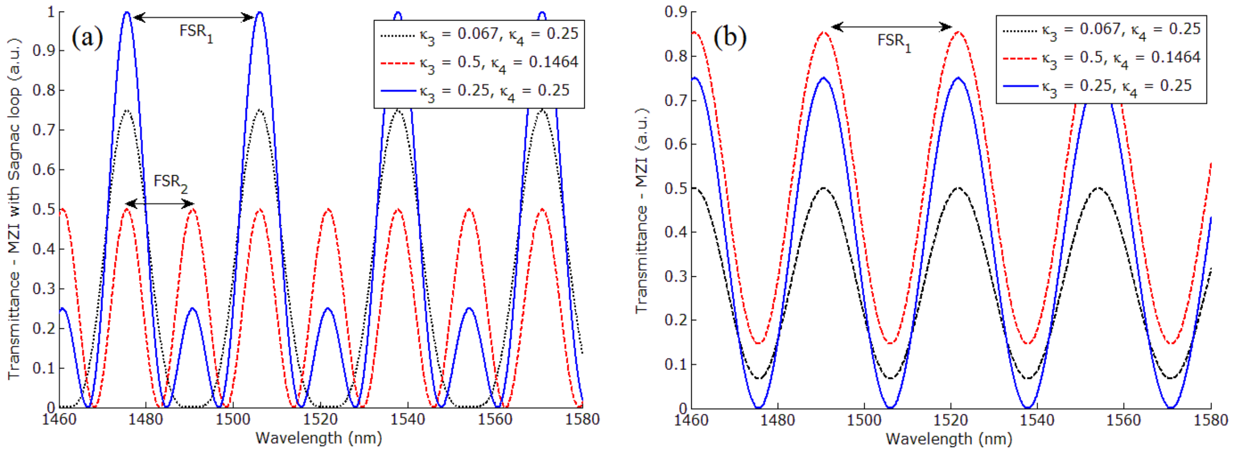

Fig. 5. Transmittances of (a) the MZI-Sagnac interferometric device and (b) the typical MZI configuration, as a function of different values of the power coupling coefficients κ_3 and κ_4.

With reference to Figs. 5(a) and 5(b), it is worth evidencing that when the power coupling coefficients κ_3 = 0.5, κ_4 = 0.1464 are set in simulations, then the typical MZI transmittance exhibits the same FSR, i.e., FSR_1 but different transmittance values. Conversely, the MZI-Sagnac transmittance plotted in Fig. 5(a), is characterized by a new FSR, i.e., FSR_2 = $FSR_1/2$ = 16.44 nm, with a maximum transmittance peak of 0.5 (a.u.). This particular behaviour, which cannot be achieved neither by a standard MZI with DCs and input and output 3 dB Y-branches [12, 14], is mainly due the presence of the Sagnac loop that generates counter-propagating signals. This results in the presence of specific double phase terms, i.e., $2\phi_u$ and $2\phi_l$, in the complex exponential functions that characterize the overall transfer function calculated by using Eqs. (2)-(5). Then, by properly setting the power coupling coefficients κ_3 and κ_4, it is possible to inhibit or exalt the presence of double-frequency components in the MZI-Sagnac overall spectral response. In conclusion, it is worth specifying that this demonstration is still valid when the device input and output ports in Figs. 5(a) and 5(b) are exchanged, and when the input and output ports are located on the same arm (i.e., upper or lower) in the typical MZI sensor (Fig. 4(b)).

Generally speaking, half the FSR of a balanced MZI can be achieved by properly setting the DC power coupling coefficients, κ_3 = 0.5, κ_4 = 0.1464, in a balanced MZI-Sagnac device.

Actually, it is worth investigating the device operation as a function of the power coupling coefficient tolerances to quantify the maximum acceptable variation of κ_3 and κ_4. To this purpose, we have calculated the spectral transmittances windowed in the wavelength range of 1470-1515 nm, by keeping, alternatively, one of the two power coupling coefficients fixed and varying the other with a step of ± 0.025 three times above and three times below its nominal value, and the results are plotted in Figs. 6(a) and 6(b). Finally, a similar investigation has been performed but considering simultaneous variations of κ_3 and κ_4 coefficients as plotted in Fig. 6(c). Actually, the latter condition is the most realistic because possible fabrication tolerances of the waveguide widths, W, and heights, H, will influence similarly both the DCs, thus inducing the same variations $\Delta\kappa_3$ and $\Delta\kappa_4$.

With reference to Fig. 6(a), it is worth noting that both positive and negative changes of κ_3 induce a non-uniform variations of the transmittance peaks. Indeed, the lateral lobes vary similarly with respect to the nominal condition as relative percentage variations of 30 % affect both peaks when κ_3 is varied from 0.425 to 0.5 ($\Delta\kappa_3 = -$ 15 %). Further, when κ_3 is varied from 0.525 to 0.575 ($\Delta\kappa_3$ = 15 %), then the relative percentage variation of both peaks is up to – 30 %. On the contrary, the central lobe, whose presence is strongly influenced by κ_3 and κ_4 as shown in Fig. 5(a), varies conversely. As plotted in Fig. 6(b), by keeping the coefficient κ_3 fixed and varying κ_4 in the range of ± 15 %, uniform transmittance peak variations of + 38 % and – 47 % occur, respectively, with respect to the nominal transmittance peak values, i.e., 0.5 (a.u.). Finally, simulations plotted in Fig. 6(c) evidence that when both the power coupling coefficients are varied simultaneously in the range of ± 15 %, then the lateral lobes are weakly influenced as overall transmittance variations of + 8.76 % and – 18.66 % occur, respectively, while the central peak undergoes huge transmittance variations of + 63.64 % and − 71.04 %, respectively. As a result of this investigation, power coupling coefficient tolerances of ± 5 % can be considered acceptable in order to ensure that FSR_2 =

$FSR_1/2$, and positive increments $+\Delta\kappa$ are generally better than $-\Delta\kappa$ to this aim. Finally, a sophisticated and flexible tool proposed by us in [26] and tested experimentally for RRs operating in the NIR [4] can be used for the rigorous design of S-bend and arc-bend DCs that characterize RR-MZI-Sagnac Vernier sensors.

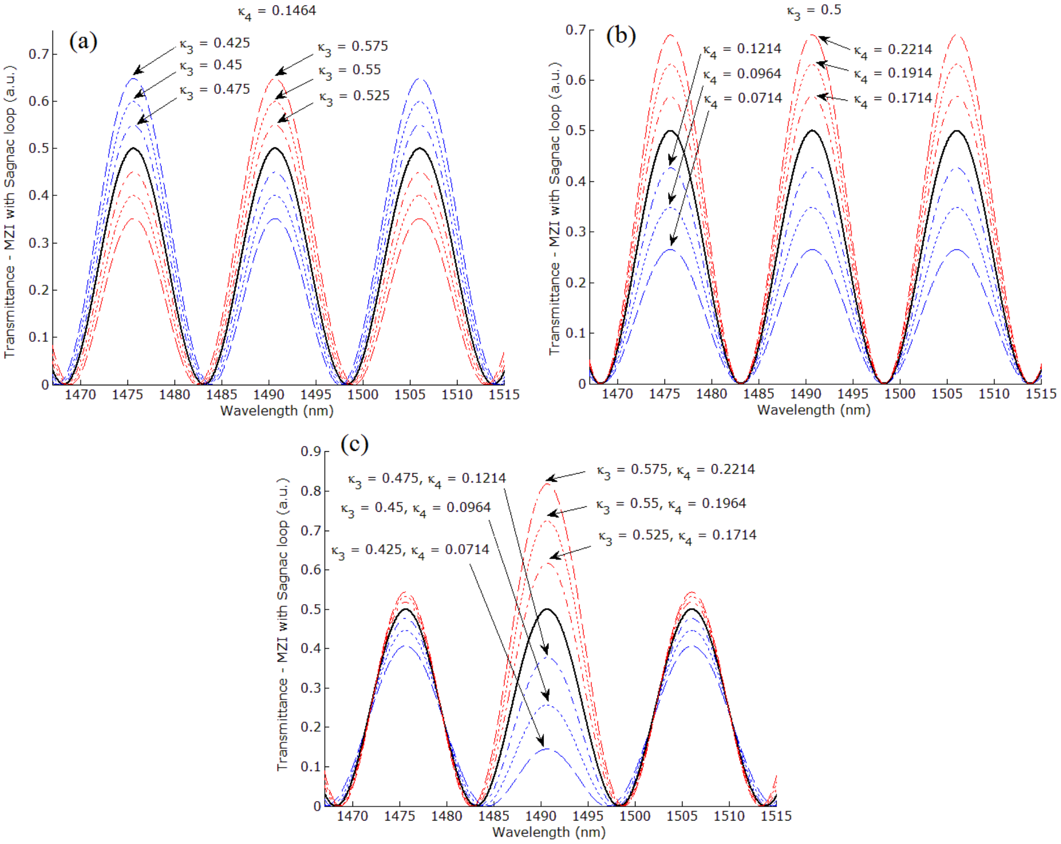

Fig. 6. Analysis of the influence of power coupling coefficients κ_3 and κ_4 on the transmittance of the balanced interferometric sensor based on a MZI and a Sagnac loop. (a) κ_4 = 0.1464 and κ_3 is varied, (b) κ_3 = 0.5 and κ_4 is varied, (c) both κ_3 and κ_4 are varied with respect to the nominal coefficients, i.e., κ_3 = 0.5, κ_4 = 0.1464. Nominal transmittances are plotted in black colour in (a), (b), and (c).

The wavelength sensitivity and LOD of the MZI-Sagnac interferometric architecture as well as of the standard MZI can be calculated by using Eqs. (8) and (9). Furthermore, it is worth noting that S_λ is the same in both the devices, while the MZI-Sagnac transmittance peaks can exhibit a $\Delta\lambda_{FWHM}$ that is half the $\Delta\lambda_{FWHM}$ of a typical MZI, resulting in a LOD that can be reduced by at least a factor two with respect to the standard MZI. For example, assuming a SNR = 10^5 and L_u = L_l = 500 µm, the wavelength sensitivity is estimated as ~ 6 μm/RIU in both the devices, while the LOD is 4.56×10^{-5} RIU in the MZI-Sagnac sensor (with power coupling coefficients κ_3 = 0.5, κ_4 = 0.1464) and 8.94×10^{-5} RIU in the typical MZI sensor (with power coupling coefficients κ_3 = 0.25, κ_4 = 0.25). Actually, the difference between the estimated LODs is due to the different full-width-at-half-maximum of the MZI-Sagnac and standard MZI transmittances, resulting in $\Delta\lambda_{FWHM} = 7.17$ nm and $\Delta\lambda_{FWHM} = 14.05$ nm, respectively.

The wavelength sensitivities, S_λ, and FSRs (i.e., FSR_1) of MZI-Sagnac (κ_3 = 0.067, κ_4 = 0.25) and standard MZI sensors have been calculated by using Eq. (8) and Eq. (12), respectively, as a function of different combinations of L_u and L_l in the case of $L_u = 0.05$ mm, $L_u = 0.5$ mm, and $L_u = 5$ mm. Finally, numerical results are shown in Figs. 7(a)-7(b).

After fixing the length L_u, we have swept the L_l length in a range of different values around L_u. As a result, asymptotic functions for S_λ and FSR have resulted from our calculations. Furthermore, the vertical asymptotes occur when denominators in Eq. (8) and Eq. (12) tend to zero, thus when $n_{g,u}L_u = n_{g,l}L_l$ or, similarly, when $L_l = \left(n_{g,u}/n_{g,l}\right)L_u$. As a result, unbalanced MZI-Sagnac or MZI devices can be preferred over the balanced configurations to enhance the wavelength sensitivity, S_λ, but resulting in longer FSRs. Moreover, by comparing Figs. 7(a)-7(b), it is evident that the longer L_u and L_l the shorter the FSR that can be achieved by keeping the ratio $n_{g,u}/n_{g,l}$ unvaried. On the contrary, the S_λ functions do not vary even when device lengths L_u and L_l of different order of magnitudes are taken into account. In conclusion, long upper and lower arm lengths allow a better light-analyte interaction and short FSR to be achieved but increasing the overall footprint of the sensor. To this purpose, a useful design strategy that can be applied consists in folding both the sensing and reference arms in Archimedean spiral paths as demonstrated in [27].

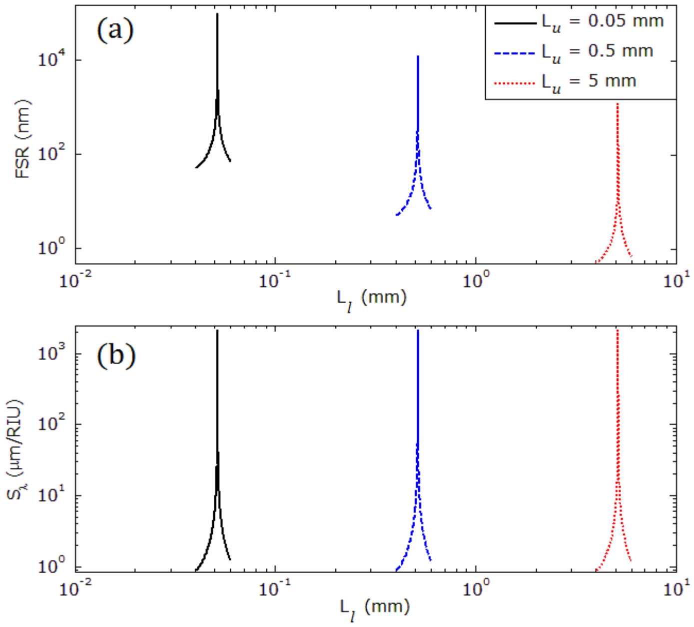

Fig. 7. (a) Free spectral range, FSR, and (b) wavelength sensitivity, S_λ, of the MZI-Sagnac and MZI sensors as a function of the lower arm length, L_l, in the case of L_u = 0.05 mm, 0.5 mm, and 5 mm.

3.1 Design of RR-MZI and RR-MZI-Sagnac Vernier sensors for chemical sensing applications

In this subsection we propose the design of Vernier sensors characterized by the cascade of a RR and balanced or unbalanced MZI-Sagnac architectures. Initially, we focus our analysis on a useful comparison between the Vernier sensor proposed here and the state-of-the-art RR-MZI Vernier sensor investigated in [14] with input and output Y-branches, with the aim to evidence the advantages that can be achieved in terms of reduced overall operative bandwidth (FSR_v) and enhanced RI sensing performance ($S_{\lambda,v}$, G_v). Hereafter, we assume lossless devices (i.e., α = 0) for two specific reasons: i) higher values of α result, predictably, in lower transmittance peaks in both RR-MZI and RR-MZI-Sagnac Vernier sensors, without influencing dramatically, the device sensing functionalities, ii) we aim at comparing RR-MZI and RR-MZI-Sagnac Vernier device transmittances as a function of geometrical and optical parameters variations whose effect cannot be simply recognizable if losses are also taken into account in simulations. Finally, we assume that both RR-MZI and RR-MZI-Sagnac sensors are covered by a SiO_2 cladding layer with the only exception of the sensitive window that is assumed to be filled with DI water.

The first analysis is related to the balanced MZI-Sagnac and MZI configurations. In particular, we have referred to Tables IV and V in [14] and set MZI and MZI-Sagnac reference and sensing arm lengths equal to $L_u = L_l$ = 6102.81 μm. Moreover, we have set balanced MZI-Segnac power coupling coefficients as κ_3 = 0.5 and κ_4 = 0.1464 to achieve half the FSR of the standard balanced MZI with input and output Y-branches as proposed in [14]. In particular, it is worth noting that both the standard MZI and MZI-Sagnac exhibit LODs of 6.72×10^{-6} RIU and 3.05×10^{-6} RIU, respectively, with SNR = 10^5 in Eq. (10), and wavelength sensitivities of S_λ = 5.89 μm/RIU calculated by using Eq. (11). Furthermore, an extended version of our sophisticated algorithmic procedure described in [13] for the design of Vernier devices based on cascaded RRs has been performed to calculate filter RR lengths useful to achieve the Vernier effect in the second operating regime in both standard RR-MZI and RR-MZI-Sagnac sensors, with both the RR power coupling coefficients, κ_1, and κ_2 equal to 0.1. Finally, the simulation results relative to the RR-MIZ-Sagnac sensor are shown in Fig. 8.

With reference to Fig. 8, it is evident that a number of Vernier configurations can be designed in order to achieve specific RI performance by selecting different values of the RR radius, R_{RR}. Moreover, a specific value of R_{RR} can be set to allow extremely high wavelength sensitivities and gains as well as ultra-low LODs to be achieved, but resulting in overall Vernier FSR of the order of 10^4-10^5 nm, thus very challenging to be employed experimentally. Consequently, very accurate strategies can be performed for the design of RR-MZI-Sagnac design by using the design maps plotted in Fig. 8. It is worth specifying that similar plots have been calculated for the design of balanced RR-MZI sensors, but different R_{RR} values have resulted since the

RR FSRs should be comparable with the standard MZI FSRs that are almost double the MZI-Sagnac FSRs characterized by κ_3 = 0.5, κ_4 = 0.1464.

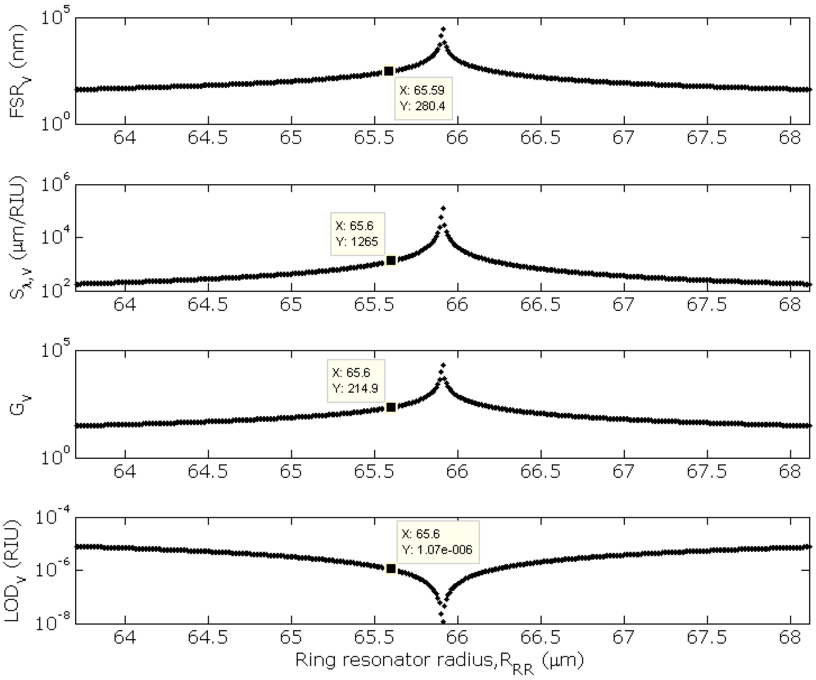

Fig. 8. RI sensing performance and Vernier FSR of the balanced RR-MZI-Sagnac sensor characterized by L_u = L_l = 6102.81 μm, plotted in log scale as a function of different RR radii.

As a result of the design procedures, we have designed a standard RR-MZI and a RR-MZI-Sagnac with geometrical and optical parameters listed in Table III. In particular, it is worth noting that RR radii of balanced RR-MZI and RR-MZI-Sagnac sensors have been chosen to achieve similar RI sensing performance in both the Vernier configurations, which are also the same reported in [14].

Table III
Geometrical and optical parameters of a standard balanced RR-MZI Vernier sensor and a balanced RR-MZI-Sagnac Vernier sensor with RI sensing performance.

Parameters	RR-MZI Vernier	RR-MZI-Sagnac Vernier
R_{RR}	32.80 μm	65.60 μm
L_{RR}	206.09 μm	412.18 μm
L_u	6102.81 μm	6102.81 μm
L_l	6102.81 μm	6102.81 μm
R_s	-	39.78 μm
FSR_{RR}	2.7073 nm	1.3537 nm
FSR_{MZI}	2.6947 nm	1.3474 nm
ΔFSR	12.6 pm	6.3 pm
G_v	214.9	214.9
FSR_v	579 nm	289.5 nm
$S_{\lambda,v}$	1265 μm/RIU	1265 μm/RIU
LOD_v	2.139×10^{-6} RIU	1.07×10^{-6} RIU

In this way, we have demonstrated that the RR-MZI-Sagnac configuration can exhibit similar Vernier wavelength sensitivities $S_{\lambda,v}$, and gains, G_v, but in half the bandwidth of the standard RR-MZI sensor. Indeed, the RR-MZI-Sagnac and RR-MZI Vernier FSRs, FSR_v, are 289.5 nm and 579 nm, respectively. Then, half the bandwidth can be saved by taking advantage of the reduced FSR of the balanced MZI-Sagnac over the standard balanced MZI, by properly setting the power coupling coefficients, κ_3 and κ_4. Moreover, the Vernier LOD that can be achieved by means of Vernier RR-MZI-Sagnac sensor is lower than RR-MZI LOD_v as reported in Table III. This is mainly due to the reduced overall Vernier peak $\Delta\lambda_{FWHM}$ as can be seen in Figs. 9(a) and 9(b), where the Vernier transmittances of the designed sensors are plotted in the NIR wavelength range of 1250-1850 nm.

By comparing Figs. 9(a) and 9(b), it is clear that the overall operative bandwidth can be halved by means of the RR-MZI-Sagnac Vernier sensor but the peak transmittance is also reduced by a factor 2 due to the particular configuration of κ_3 and κ_4 coefficients. However, we believe that this does not represent a critical aspect because the optical power that can be measured from such devices mainly depends on waveguide propagation losses and other experimental setup attenuation contributions (e.g., grating coupling efficiencies, fiber optic attenuation, etc.) that can be overcome. Finally, it is worth noting that such behaviour can be achieved for an arbitrary Vernier sensor configuration that can be selected by the design maps in Fig. 8.

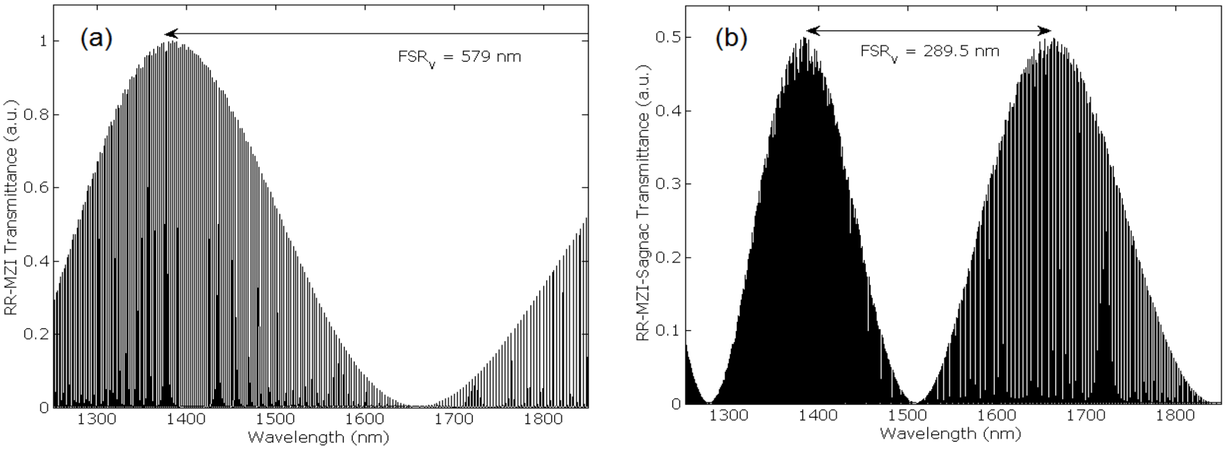

Fig. 9. Balanced (a) RR-MZI and (b) RR-MZI-Sagnac Vernier sensor transmittances with FSR_v equal to 579 nm and 289.5 nm, respectively.

A further advantage of the novel Vernier configuration proposed in this work can be demonstrated in the case on unbalanced standard MZI and MZI-Sagnac sensing devices. When designing unbalanced MZIs, similar curves as those plotted in Figs. 7(a) and 7(b) can be used in order to select the unbalancing factor between reference and sensing arms. To this purpose, we propose in Figs. 10(a) and 10(b) the FSR and S_λ design maps that are valid either for standard MZI and MZI-Sagnac devices. As an example, let us assume that the upper arm lengths in standard MZI and MZI-Sagnac devices are equal to 6102.81 μm and that the FSR_{MZI} should be 2.6 nm, similarly as reported in Table V in [14]. Consequently, in the case of the standard MZI a length of L_l = 6095 μm is suitable to this aim as shown in Fig. 10(a), resulting in S_λ = 5.683 μm/RIU. On the contrary, by taking advantage of halving the FSR by setting κ_3 = 0.5, κ_4 = 0.1464 in the unbalanced MZI-Sagnac device, a sort of "virtual" double FSR can be selected, i.e., $FSR_{MZI-Sagnac}$ = 5.210 nm with L_l = 6203 μm, as the expression for the FSR, i.e., Eq. (12), does not take into account the halving effect of κ_3 and κ_4 coefficients. Then, a lower arm length of L_l = 6203 μm corresponds to almost double the wavelength sensitivity achieved previously, i.e., S_λ = 11.37 μm/RIU. Practically, the real FSR of the unbalanced MZI-Sagnac device with κ_3 = 0.5, κ_4 = 0.1464 is equal to ~2.62 nm.

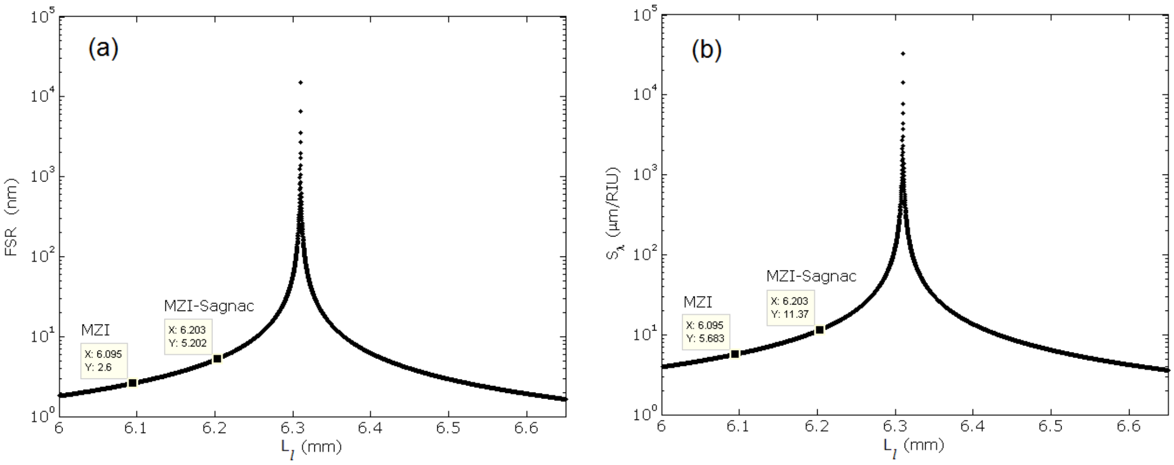

Fig. 10. (a) FSR and (b) wavelength sensitivity, S_λ, of unbalanced standard MZI and MZI-Sagnac configurations as a function of the lower arm lengths, L_l, with L_u = 6102.81 μm.

At this stage, a similar design approach already discussed and presented in Fig. 8 has been performed for both the RR-MZI and RR-MZI-Sagnac Vernier sensors, and the resulted geometrical and optical parameters have been listed in Table IV.

Table IV
Geometrical and optical parameters of a standard unbalanced RR-MZI Vernier sensor and RR-MZI-Sagnac Vernier sensor with RI sensing performance.

Parameters	RR-MZI Vernier	RR-MZI-Sagnac Vernier
R_{RR}	33.99 μm	33.92 μm
L_{RR}	213.57 μm	213.13 μm
L_u	6102.81 μm	6102.81 μm
L_l	6095.30 μm	6202.80 μm
R_s	-	39.78 μm
FSR_{RR}	2.6125 nm	2.6179 nm
FSR_{MZI}	2.6004 nm	2.6057 nm
ΔFSR	12.1 pm	12.2 pm
G_v	215.9	214.58
FSR_v	561.45 nm	559.13 nm
$S_{\lambda,v}$	1224 μm/RIU	2442 μm/RIU
LOD_v	2.135×10^{-6} RIU	1.072×10^{-6} RIU

In the case of unbalanced Vernier architectures, we demonstrate that although the RR-MZI and RR-MZI-Sagnac Vernier sensors exhibit very similar FSR_v and G_v, RI sensing performance can be doubled in the latter configuration. Indeed, the wavelength sensitivity achieved in the case of the RR-MZI Vernier sensor is 1224 μm/RIU, while that of the RR-MZI-Sagnac is 2442 μm/RIU, thus almost the double by exhibiting the same operative bandwidth as demonstrated by the FSR_v equal to 561.45 nm and 559.13 nm, respectively. Moreover, the Vernier LOD, LOD_v, of RR-MZI-Sagnac sensors is half the LOD_v of RR-MZI sensors, resulting also in an improved sensing resolution.

To give further evidence of the enhanced RI sensing performance, we propose in Figs. 11(a) and 11(b) the simulated device spectra at rest, i.e., $\Delta n_c = 0$ RIU, and when a localized RI perturbation of $\Delta n_c = 1\times10^{-4}$ RIU occurs in the sensitive area with DI water. It should be noted that the wavelength shifts can be estimated by using Eqs. (8) and (11), by considering $S_{\lambda,v} = \Delta\lambda_v/\Delta n_{eff}$. With reference to Figs. 11(a) and 11(b), the wavelength shifts of the Vernier peaks, $\Delta\lambda_v$, are as long as 244.24 nm and 122.31 nm in RR-MZI-Sagnac and RR-MZI sensors, respectively, although spectral features of both device transmittances are very similar as also confirmed by the values of FSR_v listed in Table III. Practically, the double RI sensing performance can be achieved by taking advantage of the double wavelength sensitivity, S_λ, of the unbalanced MZI-Sagnac sensing device over the standard MZI, as demonstrated in Figs. 10(a) and 10(b).

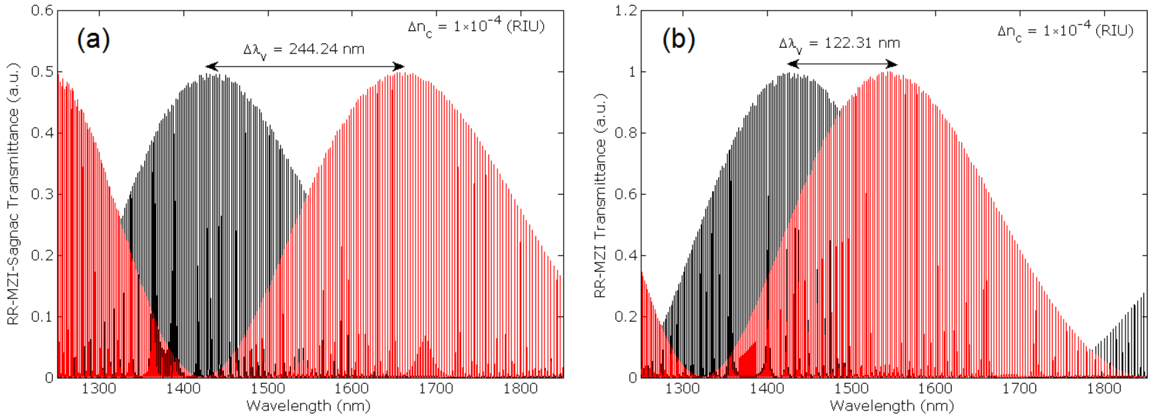

Fig. 11. Overall Vernier wavelength shifts, $\Delta\lambda_v$, induced by a cover RI variation $\Delta n_c = 1\times10^{-4}$ RIU occurring in the designed (a) RR-MZI-Sagnac and (b) RR-MZI Vernier sensors.

Finally, we show in Fig. 12, a comparison between the overall wavelength shifts occurring in the RR-MZI-Sagnac and RR-MZI Vernier sensors as a function of RI variations in DI water.

With reference to Fig. 12, it is worth noting that the enhanced sensing performance that can be achieved by using a RR-MZI-Sagnac Vernier sensors are represented by the improved overall LOD_v, as wavelength shifts occur firstly in the RR-MZI-Sagnac sensor, and sensor dynamic response as the RR-MZI-Sagnac longest wavelength shift due to Δn_c = 1×10^{-4} RIU is at a wavelength of 1676 nm, over 1554 nm occurring in the RR-MZI sensor. Apparently, the wider RR-MZI-Sagnac sensor dynamic could be considered as a drawback in terms of required operating sensor bandwidth but, practically, this is not properly correct as double wavelength sensitivities represent a concrete advantage when small RI variations occur, e.g., 10^{-8}-10^{-5} RIU, depending on the LOD.

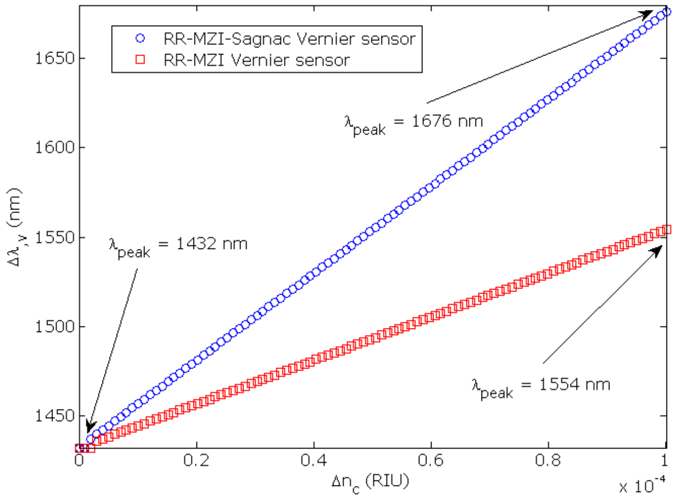

Fig. 12. Overall Vernier wavelength shifts, $\Delta\lambda_v$, for RR-MZI-Sagnac and RR-MZI Vernier sensors as a function of RI variations in DI water and plotted in log scale.

In conclusion, the design approach described is obviously scalable to other RR-MZI-Sagnac configurations that can exhibit shorter Vernier FSRs, and still exhibiting double sensing performance with respect to the standard RR-MZI sensors. By referring to the optimized RR-MZI Vernier sensors proposed in [14] for CO_2 and NH_3 detection in air and DI water, respectively, the double RI sensing performance achieved by the unbalanced RR-MZI-Sagnac Vernier sensors allow CO_2 gas concentrations lower than 5,000 ppm and NH_3 concentrations in the 0-30,000 ppm range to be detected, still exhibiting the same operating bandwidths of RR-MZI sensors, as listed in Table IV. Alternatively, similar performance demonstrated theoretically in [14] by RR-MZI Vernier sensors can be achieved with half their Vernier FSR by designing balanced MZI-Sagnac architectures, as reported in Table III.

The investigation of the new sensing configuration proposed in this work is completed by analysing the operation of the RR-MZI-Sagnac sensor, whose design and optical parameters are listed in Table III, as a function of κ_3 and κ_4 power coupling coefficient tolerances as already proposed for the MZI-Sagnac device and shown in Fig. 6. To this purpose, we have simulated the sensor spectrum at rest (i.e., Δn_c = 0 RIU) as plotted in Fig. 11(a), by taking into account simultaneous variations of $\Delta\kappa_3 = \Delta\kappa_4 = -$ 15 %, i.e., Fig. 13(a), $\Delta\kappa_3 = \Delta\kappa_4 =$ + 15 %, i.e., Fig. 13(c), with respect to the nominal coefficient values κ_3 = 0.5, κ_4 = 0.1464, i.e., Fig. 13(b). Numerical results, plotted in the wavelength range of 1250-1720 nm, demonstrate that the overall Vernier peak still preserves its shape when a maximum κ_3 and κ_4 negative variation of $-$ 15 % occur, but its spectral lines undergo an overall decrease. In particular, as evidenced by the darker peak-shape in Fig. 13(a), the peaks that allow the half FSR_{MZI} to be achieved decrease also according to simulations shown in Fig. 6(c), while the remaining spectral lines undergo a transmittance decrease of 20 % with respect to the Vernier spectrum with nominal power coupling coefficients (Fig. 13(b)). Conversely, when a maximum κ_3 and κ_4 positive variation of + 15 % occur, the spectral lines constituting the darker peak-shape increase as shown with Fig. 6(c), while the remaining spectral lines undergo an overall transmittance increase up to 60 % with respect to the Vernier spectrum plotted in Fig. 13(b). As a result of this analysis, positive power coupling coefficient variations are confirmed as more tolerant than negative $\Delta\kappa$. Furthermore, the different transmittance peaks characterizing spectral lines of the overall Vernier peak do not influence the RI sensing performance as nominal LOD_v and $S_{\lambda,v}$ as listed in Table IV can be achieved. It is worth specifying that, when completely different power coupling coefficients are taking into account in balanced and unbalanced RR-MZI-Sagnac Vernier configurations, e.g., κ_3 = 0.067 and κ_4 = 0.25 (see also Fig. 5(a)), the spectral features of the Vernier spectra become those of a standard RR-MZI sensor, thus losing the advantages of halving the overall operating bandwidth and achieving double RI sensing performance, respectively.

In conclusion, by comparing the architectures of the standard RR-MZI and RR-MZI-Sagnac sensors, the main difference is related to the presence of a signal, namely S_{in}^{-}, that is generated by the Sagnac loop and propagates back to the input port as shown in Fig. 2. Actually, this specific signal seems not to affect the device operation as experimentally demonstrated in silica microwire-based MZI-Sagnac electric field sensors [28] and in integrated wavelength and bandwidth-tunable silicon comb filters [29]. Anyway, we demonstrate in Fig. 14 that the signal S_{in}^{-} in a high-performance RR-MZI-Sagnac Vernier sensor can be dramatically minimized by properly setting the RR power coupling coefficients, κ_1 and κ_2. In particular, by setting κ_1 = 0.01 and κ_2 = 0.1 the S_{in}^{-} transmittance can be decreased of more than 95 % with respect to the configuration with κ_1 = 0.1 and κ_2 = 0.1, but resulting in a decrease of the output signal, S_{out}, of about 62 %. However, although a 62 % of S_{out} decrease can be acceptable depending on the waveguide propagation losses affecting the overall sensor, optimization procedures can be performed to figure out the pair of coefficients κ_1 and κ_2 that allow the signal S_{in}^{-} to be reduced without influencing dramatically S_{out}.

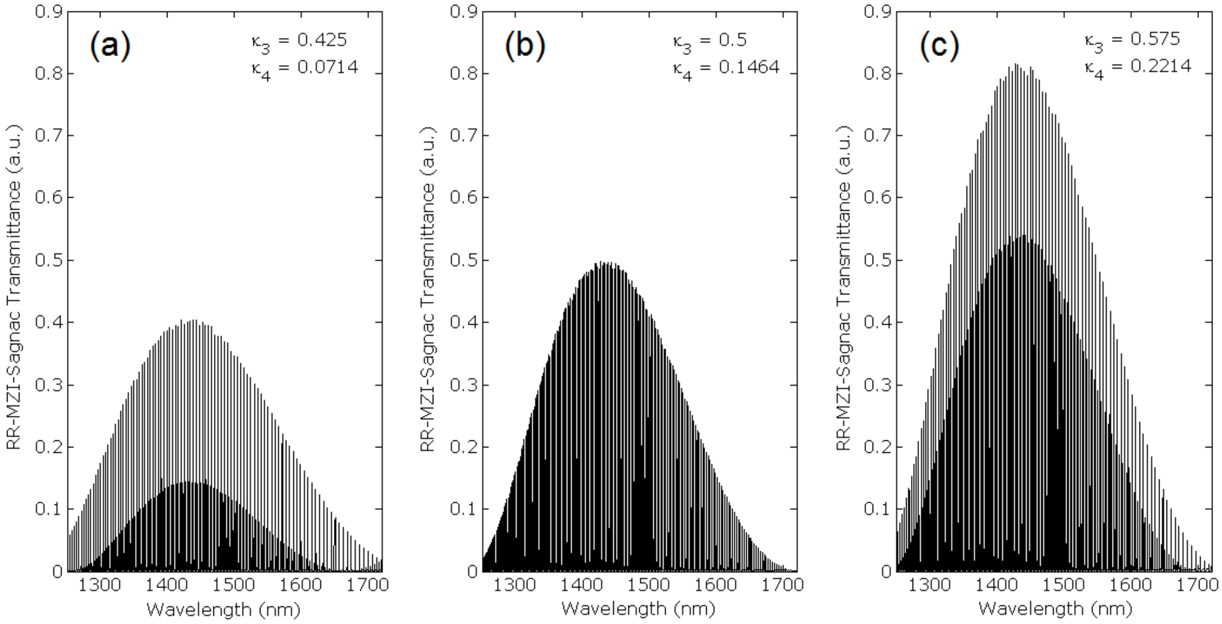

Fig. 13. RR-MZI-Sagnac Vernier sensor transmittances as a function of different values of power coupling coefficients κ_3 and κ_4; (a) κ_3 = 0.425, κ_4 = 0.0715, (b) κ_3 = 0. 5, κ_4 = 0.1464, (c) κ_3 = 0.575, κ_4 = 0.2214.

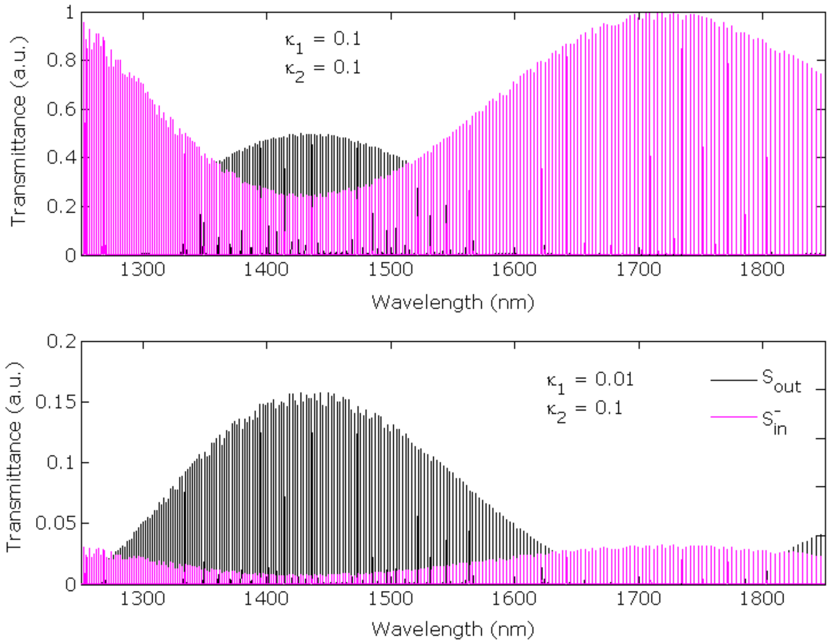

Fig. 14. S_{out}.and S_{in}^{-} signals in a RR-MZI-Sagnac Vernier sensor as a function of different values of the power coupling coefficients κ_1 and κ_2; (top) κ_1 = 0.1 and κ_2 = 0.1, (bottom) κ_1 = 0.01 and κ_2 = 0.1.

4. Conclusion

In this paper, we have investigated theoretically a new SOI integrated photonic sensor based on cascaded RR and MZI-Sagnac interferometric configuration for ultra-high performance RI sensing in the NIR wavelength range, suitable for chemical and biochemical applications. Actually, we have demonstrated that by designing balanced MZI-Sagnac architectures with DC power coupling coefficients κ_3 = 0.5 and κ_4 = 0.1464, the RR-MZI-Sagnac Vernier sensors can exhibit similar wavelength sensitivities and LODs as those achievable by state-of-the-art RR-MZI Vernier sensors, but with half their operating bandwidths, or, in other words, exhibiting half their overall Vernier FSRs. Alternatively, when the RR-MZI-Sagnac Vernier sensors are designed with unbalanced MZI-Sagnac architectures and power coupling coefficients κ_3 = 0.5 and κ_4 = 0.1464, then we have demonstrated that double RI sensing performance can be achieved with respect to state-of-the-art RR-MZI Vernier sensors, still exhibiting their Vernier FSRs, which is a remarkable advantage when working with Vernier sensing configurations as the higher the RI sensing performance the longer the envelope Vernier transmittance FSR. In this context, we have presented a detailed theoretical investigation of power coupling coefficient tolerances and numerical results have revealed that variations of ± 5 % with respect to the nominal values previously mentioned can be considered acceptable in order to ensure the proper device operation. However, even in the case larger variations of κ_3 and κ_4 occur, numerical results demonstrate that the overall Vernier envelops and sensing performance are preserved in both balanced and unbalanced RR-MZI-Sagnac design approaches. Moreover, we have investigated the influence of the counter-propagating signals generated into the Sagnac loop and find out that specific configuration of the RR DCs, e.g., κ_1 = 0.01 and κ_2 = 0.1, can be used for decreasing the backward signal at the input port down to 95 %. Finally, we believe that the RR-MZI-Sagnac Vernier devices proposed in this work can be advantageous for the design of ultra-high performance Vernier sensors characterized by small footprints as shorter arm lengths than state-of-the-art RR-MZI Vernier sensors need to be designed and fabricated. Moreover, the experimental demonstration of such devices would pave the way for mid-infrared sensing applications and real-time, label-free spectroscopic functionalities. In fact, the Vernier effect in SOI and germanium-on-silicon (GOS) cascaded RRs has been already demonstrated around 3.8 μm [30, 31], exhibiting a very good agreement with theoretical results, that were calculated by using the modelling and design tools proposed in this work. In conclusion, simulations reveal that NH_3 concentrations in the 0-30,000 ppm range and CO_2 traces lower than 5,000 ppm can be detected in DI water and air, respectively, by optimized RR-MZI-Sagnac Vernier sensors operating at NIR wavelengths around 1.55 μm.

References

[1] V. M. N. Passaro, C. de Tullio, B. Troia, M La Notte, G. Giannoccaro, F. De Leonardis, Recent advances in integrated photonic sensors, Sensors 12 (2012) 15558–15598.

[2] V. M. N. Passaro, B. Troia, M. La Notte, F. De Leonardis, Photonic resonant microcavities for chemical and biochemical sensing, RCS Adv. 3 (2013) 25–44.

[3] M. La Notte, B. Troia, T. Muciaccia, C. E. Campanella, F. De Leonardis, V. M. N. Passaro, Recent advances in gas and chemical detection by Vernier effect-based photonic sensors, Sensors 14 (2014) 4831–4855.

[4] B. Troia, A. Z. Khokhar, M. Nedeljkovic, S. A. Reynolds, Y. Hu, G. Z. Mashanovich, and V. M. N. Passaro, Design procedure and fabrication of reproducible silicon Vernier devices for high-performance refractive index sensing, Sensors 15 (2015) 13548–13567.

[5] L. Jin, M. Li, J.-J. He, Highly-sensitive silicon-on-insulator sensor based on two cascade micro-ring resonators with Vernier effect, Opt. Commun. 284 (2011) 156–159.

[6] J. Hu, D. Dai, Cascaded-ring optical sensor with enhanced sensitivity by using suspended Si-nanowires, IEEE Photon. Technol. Lett. 23 (2011) 842–844.

[7] X. Jiang, J. Ye, J. Zou, M. Li, J.-J He, Cascaded silicon-on-insulator double-ring sensors operating in high-sensitivity transverse-magnetic mode. Opt. Lett. 38 (2013) 1349–1351.

[8] T. Claes, W. Bogaerts, P. Bienstman, Experimental characterization of a silicon photonic biosensor consisting of two cascaded ring resonator based on the Vernier-effect and introducing of a curve fitting method for an improved detection limit, Opt. Express 18 (2010) 22747–22761.

[9] T. Claes, W. Bogaerts, P. Bienstman, Vernier-cascade label-free biosensor with integrated arrayed waveguide grating for wavelength interrogation with low-cost broadband source, Opt. Lett. 36 (2011) 3320–3322.

[10] V. Zamora, P. Lützow, M. Weiland, D. Pergande, Investigation of cascaded SiN microring resonators at 1.3 μm and 1.5 μm, Opt. Express 21 (2013) 27550–27557.

[11] X. Tu, J. Song, T.-Y. Liow, M. K. Park, J. Q. Yiying, J.S. Kee, M. Yu, G.-Q. Lo, Thermal independent Silicon-Nitride slot waveguide biosensor with high sensitivity, Opt. Express 20 (2012) 2640–2648.

[12] X. Jiang, Y. Chen, F. Yu, L. Tang, M. Li, J.-J. He, High-sensitivity optical biosensor based on cascaded Mach-Zehnder interferometer and ring resonator using Vernier effect, Opt. Lett. 39 (2014) 6363–6366.

[13] V. M. N. Passaro, B. Troia, F. De Leonardis, A generalized approach for design of photonic gas sensors based on Vernier-effect in mid-IR, Sens. Actuators B Chem. 168 (2012) 402–420.

[14] M. La Notte, V. M. N. Passaro, Ultra-high sensitivity chemical photonic sensing by Mach-Zehnder interferometer enhanced Vernier-effect, Sens. Actuators B Chem. 176 (2013) 994–1007.

[15] C. Han, H. Ding, F. Lv, Demonstration of a refractrometric sensor based on an optical micro-fiber three-beam interferometer, Sci. Rep. 4 (2014) 1–7.

[16] W. Bogaerts, P. De Heyn, T. Van Vaerenbergh, K. De Vos, S. K. Selvaraja, T. Claes, P. Dumon, P. Bientsman, D. Van Thourhout, R. Baets, Silicon microring resonators, Laser Photon. Rev. 6 (2012) 47–73.

[17] F. Dell'Olio, V. M. N. Passaro, Optical sensing by optimizing silicon slot waveguides, Opt. Exp. 15 (2007) 4977-4993.

[18] D. K. C. Wu, K. J. Lee, V. Pureur, B. T. Kuhlmey, Performance of refractive index sensors based on directional couplers in photonic crystal fibers, J. Lightw. Technol. 31 (2013) 3500–3510.

[19] I. M. White, X. Fan, On the performance quantification of resonant refractive index sensors, Opt. Exp. 16 (2008) 1020–1028.

[20] Y. Sun, X. Fan, Optical ring resonators for biochemical and chemical sensing, Anal. Bioanal. Chem. 399 (2011) 205–211.

[21] Comsol Multhyphysics by COMSOL$^{\copyright}$, ver 3.2, single license, 2005.

[22] H. H. Li, Refractive index of silicon and germanium and its wavelength and temperature derivatives, J. Phys. Chem. Ref. Data 9 (1980) 561–658.

[23] I. H. Malitson, Interspecimen comparison of the refractive index of fused silica, J. Opt. Soc. Am. 55 (1965) 1205-1208.

[24] G. M. Hale, M. R. Querry, Optical constants of water in the 200-nm to 200-μm wavelength region, Appl. Opt. 12 (1973) 555–563.

[25] J. Soler Penadés, C. Alonso-Ramos, A. Z. Khokhar, M. Nedeljkovic, L. A. Boodhoo, A. Ortega-Moñux, I. Molina-Femández, P. Cheben, G. Z. Mashanovich, Opt. Lett. 39 (2014) 5661–5664.

[26] B. Troia, F. De Leonardis, V. M. N. Passaro, Generalized modelling for the design of guided-wave optical direcitonal couplers, Opt. Lett. 39 (2014) 1161–1164.

[27] M. Nedeljkovic, S. Stankovic, C. J. Mitchell, A. Z. Khokhar, S. A. Reynolds, D. J. Thomson, F. Y. Gardes, C. G. Littlejohns, G. T. Reed, G. Z. Mashanovich, Mid-infrared thermo-optic modulators in SOI, IEEE Photon. Technol. Lett. 26 (2014) 1352–1355.

[28] C. Han, F. Lv, C. Sun, H. Ding, Silica microwire-based interferometric electric field sensor, Opt. Lett. 40 (2015) 3683–3686.

[29] X. Jiang, J. Wu, Y. Yang, T. Pan, J. Mao, B. Liu, R. Liu, Y. Zhang, C. Qiu, C. Tremblay, Y. Su, Wavelength and bandwidth silicon comb filter based on Sagnac loop mirrors with Mach-Zehnder interferometer couplers, Opt. Exp. 24 (2016) 2183–2188.

[30] B. Troia, A. Z. Khokhar, M. Nedeljkovic, J. Soler Penadés, V. M. N. Passaro, G. Z. Mashanovich, Cascade-coupled racetrack resonators based on the Vernier effect in the mid-infrared, Opt. Exp. 22 (2014) 23990–24003.

[31] B. Troia, J. Soler Penadés, A. Z. Khokhar, M. Nedeljkovic, C. Alonso-Ramos, V. M. N. Passaro, G. Z. Mashanovich, Germanium-on-silicon Vernier-effect photonic microcavities for the mid-infrared, Opt. Lett. 41 (2016) 610–613.

Biographies

Benedetto Troia received his Laurea Degree (*cum laude*) in Electronic Engineering in 2011 from Politecnico di Bari, Italy, and his Ph.D. in Electrical and Information Engineering from Inter-Polytechnic Doctorate School in 2015. Actually he is working with Photonics Research Group and his research interests are mainly in the fields of integrated optical sensors, mid-infrared photonics and nonlinear photonic devices. He is coauthor of more than thirty papers in international journals and conference proceedings.

Francesco De Leonardis received his Laurea degree and his Ph.D. in Electronic Engineering from Politecnico di Bari in 1999 and 2003, respectively. Since 2004 he is research assistant at Politecnico di Bari, Italy, and a member of Photonics Research Group. His research interests are mainly in the fields of integrated optical sensors and nonlinear photonic devices. He is author or co-author of more than 100 papers in international journals and conference presentations and the holder of one international patent.

Vittorio M. N. Passaro (S'92, SM'05) received his Laurea Degree *cum laude* in Electronic Engineering at University of Bari in February 1988, and his Ph.D. in Electronic Engineering, curriculum Optoelectronics, in July 1992. Since October 2000 he joined Politecnico di Bari as associate professor of Electronics. Since 2004 he formed and leads the Photonics Research Group at Politecnico di Bari. He is author or co-author of more than 300 papers published in international journals (one by Nature Photonics) and conference proceedings. He is also the holder of two international patents and the Editor of three scientific books (one by Springer). Dr. Passaro is a Senior Member of Optical Society of America, and an Associate Member of the National Institute of Nuclear Physics (INFN).